



Article

High-Temperature Quantum Hall Effect in Graphite-Gated Graphene Heterostructure Devices with High Carrier Mobility

Siyu Zhou [†], Mengjian Zhu ^{*,†}, Qiang Liu, Yang Xiao, Ziru Cui and Chucai Guo ^{*,ID}

College of Advanced Interdisciplinary Studies & Hunan Provincial Key Laboratory of Novel Nano-Optoelectronic Information Materials and Devices, National University of Defense Technology, Changsha 410073, China

* Correspondence: zhumengjian11@nudt.edu.cn (M.Z.); gcc_1981@163.com (C.G.)

[†] These authors contributed equally to this work.

Abstract: Since the discovery of the quantum Hall effect in 1980, it has attracted intense interest in condensed matter physics and has led to a new type of metrological standard by utilizing the resistance quantum. Graphene, a true two-dimensional electron gas material, has demonstrated the half-integer quantum Hall effect and composite-fermion fractional quantum Hall effect due to its unique massless Dirac fermions and ultra-high carrier mobility. Here, we use a monolayer graphene encapsulated with hexagonal boron nitride and few-layer graphite to fabricate micrometer-scale graphene Hall devices. The application of a graphite gate electrode significantly screens the phonon scattering from a conventional SiO₂/Si substrate, and thus enhances the carrier mobility of graphene. At a low temperature, the carrier mobility of graphene devices can reach 3×10^5 cm²/V·s, and at room temperature, the carrier mobility can still exceed 1×10^5 cm²/V·s, which is very helpful for the development of high-temperature quantum Hall effects under moderate magnetic fields. At a low temperature of 1.6 K, a series of half-integer quantum Hall plateaus are well-observed in graphene with a magnetic field of 1 T. More importantly, the $\nu = \pm 2$ quantum Hall plateau clearly persists up to 150 K with only a few-tesla magnetic field. These findings show that graphite-gated high-mobility graphene devices hold great potential for high-sensitivity Hall sensors and resistance metrology standards for the new Système International d'unités.

Keywords: Graphene; hBN; heterostructure; field-effect devices; carrier mobility; quantum Hall effect



Citation: Zhou, S.; Zhu, M.; Liu, Q.; Xiao, Y.; Cui, Z.; Guo, C.

High-Temperature Quantum Hall Effect in Graphite-Gated Graphene Heterostructure Devices with High Carrier Mobility. *Nanomaterials* **2022**, *12*, 3777. <https://doi.org/10.3390/nano12213777>

Academic Editor: Jean-Pierre Bucher

Received: 28 September 2022

Accepted: 22 October 2022

Published: 26 October 2022

Publisher's Note: MDPI stays neutral with regard to jurisdictional claims in published maps and institutional affiliations.



Copyright: © 2022 by the authors. Licensee MDPI, Basel, Switzerland. This article is an open access article distributed under the terms and conditions of the Creative Commons Attribution (CC BY) license (<https://creativecommons.org/licenses/by/4.0/>).

1. Introduction

The quantum Hall effect (QHE) is a perfect phenomenon that reflects the microscopic quantum physics behavior in the mesoscopic scale. It has attracted great attention since it was discovered in 1980 [1]. Charged particles moving rapidly along the edge channels are not affected by impurities or disorders, forming a one-dimensional conductive channel with quantum conductivity of e^2/h . Considering that Landau levels are discrete, each Landau level will form an edge channel, so the number of Landau levels or filling factors that have been filled determines the quantized Hall conductance [2], and the Hall resistance platform at this time corresponds to $(h/e^2)/n$. Since the quantum Hall resistance is determined by Planck constant h and the basic constant e of electron charge, it also leads to the establishment of a new resistance measurement standard. At present, the standard is implemented in GaAs/AlGaAs heterostructure devices [3], which usually require the experimental magnetic field strength $B \approx 10$ T and measurement under the condition of $T \approx 1.3$ K [4,5]. This experimental condition requires low-temperature liquid-helium and a very strong magnetic system, which is very strict for realistic applications. Alternatively, the quantum anomalous Hall effect (QAHE) [6–9], the quantum case of the anomalous Hall effect [10–12], is a transport phenomenon where the Hall resistance is quantized to the von Klitzing constant due to the spontaneous magnetization of a ferromagnetic material even at zero magnetic field. Similar to the QHE under strong magnetic fields, the quantized

Hall resistance of QAHE is also supposed to be universal, independent of the experimental details. However, the quantization accuracy of QAHE reported so far is much worse than that of QHE [13–15]. In addition, in the present study, all the precision measurements of QAHE were performed at extremely low temperatures below 300 mK [16]. To make the QAHE-based resistance standard more practical, a further increase in the operating temperature would be required.

Recently, a more accurate and practical quantum Hall resistance standard has been rapidly developed by utilizing the unique electronic characteristics of graphene [17–21]. Compared with traditional GaAs/AlGaAs heterostructure devices, graphene devices can observe the QHE at higher temperatures and lower magnetic fields [22]. The reason why graphene can show QHE in a low magnetic field is that the energy interval between the first two Landau levels [21,23] is $\Delta E_{\text{Graphene}} = 36\sqrt{B} \text{ meV/T}^{1/2}$, which is much larger than $\Delta E_{\text{GaAs}} = 1.7B \text{ meV/T}$ of traditional GaAs/AlGaAs heterostructure devices [22]. Therefore, the Hall resistance of graphene can be accurately quantified to $h/(2e^2)$ in such a low magnetic field. However, to achieve such accuracy, graphene quantum Hall devices also need to have high carrier mobility. Previous studies have shown that graphene devices with a carrier mobility of $1.5 \times 10^4 \text{ cm}^2/\text{V}\cdot\text{s}$ can exhibit good QHE at $T = 4 \text{ K}$ and $B = 14 \text{ T}$, and they discovered the QHE in graphene occurs at a half-integer filling factor [23]. Additionally, chemical vapor deposition (CVD) grown graphene [24] with a high carrier mobility of $6 \times 10^5 \text{ cm}^2/\text{V}\cdot\text{s}$ shows a fractional quantum Hall effect (FQHE) at $T = 0.3 \text{ K}$ and $B = 12 \text{ T}$. Room-temperature QHE [25] is early discovered at a very large magnetic field of $B = 45 \text{ T}$. Therefore, in order to achieve higher performance of graphene quantum Hall devices under relaxed conditions, high carrier mobility is required. Recently, the discovery of other two-dimensional (2D) crystals, such as hexagonal boron nitride (hBN), leads to the emergence of a van der Waals (vdW) heterostructure using a layer-to-layer assemble strategy. The properties of vdW heterostructures can be precisely controlled by adjusting the type of 2D component materials, the number of layers, and the band alignment, which is critical from both fundamental and application points of view. For instance, it has been shown that the hBN encapsulation significantly reduces the scattering in graphene and thus dramatically enhances the carrier mobility of graphene [26–28]. The vdW heterostructure that combining hBN and graphene have led to the discovery of many exciting phenomena including Hofstadter's butterfly, Coulomb drag, and fractional quantum Hall effect, as well as many functional devices such as tunneling field-effect transistors [29–33].

Here, we fabricate a monolayer graphene (MLG) Hall device encapsulated with hBN, the fabrication process is shown in Supplementary Material Section 1. The device uses few-layer graphite (FLG) as gate electrodes and one-dimensional Cr/Au edge electrodes. By utilizing the advanced graphite gate device architecture, the hBN/MLG/hBN vdW heterostructure device demonstrates ultra-high carrier mobility at both room temperature and low temperature, leading to observation of the QHE at an elevated temperature of 150 K and a moderate magnetic field below 8 T. Our results show that for metrology, this may provide a new idea for quantizing Hall resistance benchmark [34]; and for magnetic field detection, graphene also has significant performance advantages in the field of Hall sensors with ultra-high sensitivity [35].

2. Results and Discussions

Figure 1a shows the optical image of the device. Our graphene device is made of vdW heterostructure on a silicon substrate as it shows in Figure 1b. The heterostructure is mainly composed of exfoliated MLG, which is encapsulated with hBN as the dielectric layer. The Raman spectra of hBN/MLG/hBN is shown in Figure 1c, the characteristic peak of hBN is at 1366 cm^{-1} and the characteristic G and 2D peak of monolayer graphene is at 1578 cm^{-1} and 2678 cm^{-1} , respectively. We notice the G peak intensity of graphene is rather low due to the coverage of hBN, but the 2D peak is symmetrical, which accords with the Raman 2D peak of monolayer graphene. The low charged defect density in hBN can improve the carrier mobility [36], and then FLG is used as the graphite-gated electrode to shield

the disorder of charged impurities in the silicon substrate [37], which can also improve the carrier mobility and reduce the inhomogeneity of charge [38,39]. At the same time, in order to reduce the contact resistance between graphene and metal electrode and realize the accurate measurement of the QHE, we use a one-dimensional edge contact method to realize the ability of high-quality electrical contact [28]. Compared with conventional surface contact [40–43], edge contact can reduce the doping of graphene in the process of metal evaporation [44,45], and can effectively reduce the contact resistance, so as to achieve high electronic performance [46] and make the carrier mobility of graphene devices close to the limit [21].

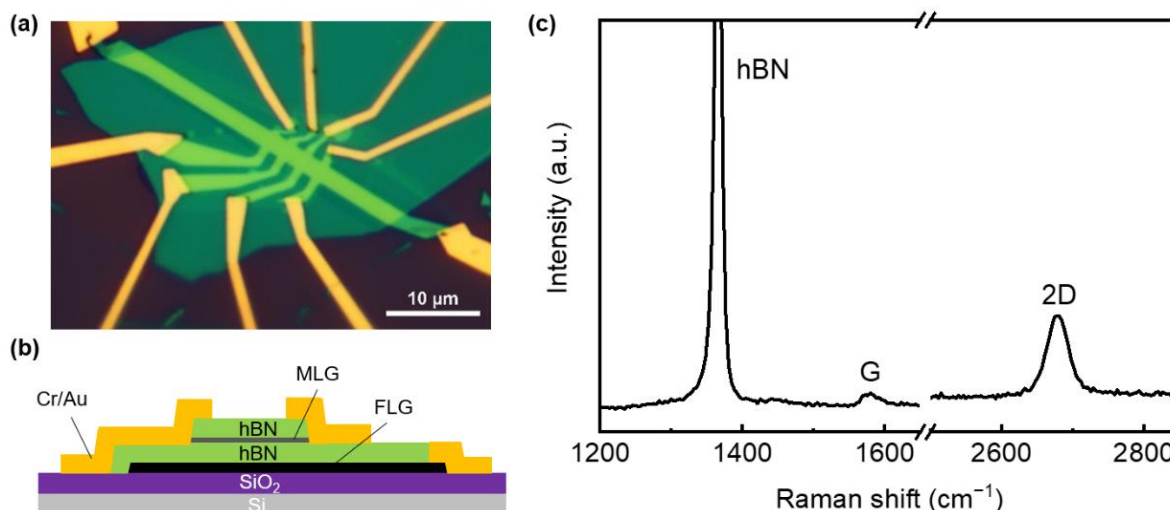


Figure 1. (a) Optical microscope image of the graphene quantum Hall device. (b) Schematic of the cross-section view of the hBN/MLG/hBN vdW heterostructure device. (c) Raman spectra of the hBN/MLG/hBN vdW heterostructure. The wavelength of laser is 532 nm, see Supplementary Material Section 2.

We first measured the electronic transport properties of the device at room temperature (290 K) and low temperature (1.6 K) by using standard low-frequency locking technology under small ac bias (100 nA) to measure the four-probe longitudinal (R_{xx}) and Hall resistance (R_{xy}) and applied the graphite-gate voltage V_g to adjust the carrier density, the measurement set-up is shown in Figure S3. Figure 2a,d plot the longitudinal resistance of graphene as a function of applied gate voltage ($R_{xx}-V_g$) under room temperature (290 K) and low temperature (1.6 K). The gate voltage changes the carrier concentration n and thus the resistance of graphene through the capacitance of MLG/hBN/FLG. In consideration of the thickness of the bottom hBN flake, a graphite-gate capacitance per area A of $C_g/A = \epsilon_0 \epsilon_r / e d_{\text{hBN}} \approx 6 \times 10^{11} \text{ cm}^{-2} \text{ V}^{-1}$, where ϵ_0 is the dielectric constant, $\epsilon_r \approx 3.9$ is the relative permittivity of hBN, e is the electron charge and $d_{\text{hBN}} = 36 \text{ nm}$ is the thickness of the bottom hBN flake [47]. In Figure 2a, the device showed the charge-neutrality point (Dirac point, DP) situated close to zero gate voltage, $V_{\text{DP}} = -0.17 \text{ V}$ at room temperature $T = 290 \text{ K}$. The intensity of the peak in Figure 2a,d represents the largest resistance of graphene at the DP of graphene, while the width of the peak represents the broadening of the DP, mainly caused by the electron-hole puddles in our devices. For graphene near the DP, the concentration of thermally excited carriers Δn_T can be estimated as: $(T/\hbar v_F)^2$, where T is temperature, \hbar is reduced Planck constant, and v_F is Fermi velocity. Therefore, the resistance at DP increases with decreasing temperature, as shown in Figure 2a,d.

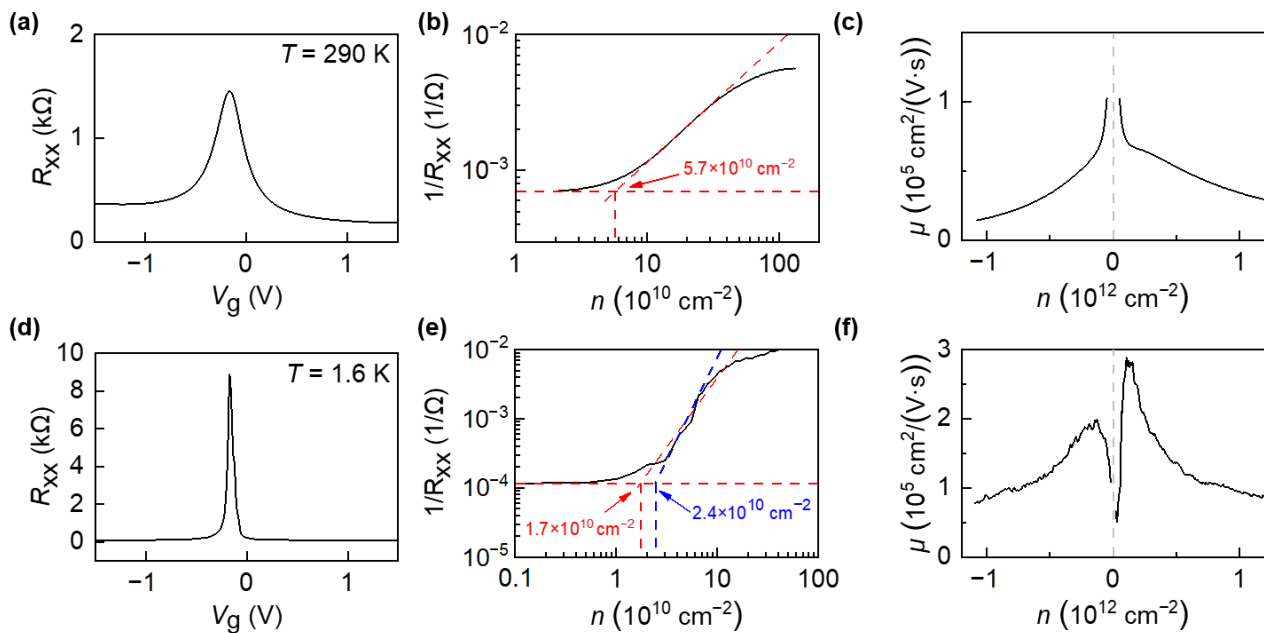


Figure 2. (a) Longitudinal resistance R_{xx} as a function of gate voltage (V_g) at 290 K under small ac bias current (100 nA). (b) The inverse longitudinal resistance R_{xx} as a function of the charge carrier density n . The residual charge carrier fluctuation is calculated by the intercept of two lines. (c) Carrier mobility μ as function of charge carrier density n for $|n| > 5.7 \times 10^{10}$ cm $^{-2}$. (d,e) Same as (a,b), but measured at $T = 1.6$ K. (f) Carrier mobility μ as a function of charge carrier density n for $|n| > 1.7 \times 10^{10}$ cm $^{-2}$ – 2.4×10^{10} cm $^{-2}$.

The width of the R_{xx} peak represents the broadening of the DP, namely, how closely can one approach the DP in graphene. Many theoretical works predict that graphene exhibit $\sigma_{min} = e^2/h$ even at vanishing charge density, the DP. However, in a realistic sample charged impurities or structural disorder break up the carrier system into puddles of electrons and holes for V_g near the V_{DP} . As a result, the combined (electron plus hole) carrier density in “dirty” graphene never drops below a value Δn , referred to as inhomogeneity density. Both the thermally activated carriers and phonon scattering process increase with increasing temperature, leading to a broadened Δn and width of the R_{xx} - V_g peak in Figure 2. In Figure 2a,d, the experimental observation that the peak widths increase and the intensity decrease with the increase of the temperature are in good agreements with previous reports in high-quality graphene devices.

The residual charge carrier fluctuation is $n^* = 5.7 \times 10^{10}$ cm $^{-2}$ and the charge carrier mobility μ is calculated by using Drude formula $\sigma = ne^2\tau/m$, where σ is the electrical conductivity [48]. It can be observed that the mobility of the device can reach around 1×10^5 cm 2 /V s, see Figure 2c. Then, we cooled down the device in a ^4He cryostat system to 1.6 K, the residual charge carrier fluctuation decreases to 1.7×10^{10} cm $^{-2}$ \sim 2.4×10^{10} cm $^{-2}$ and the mobility increases to 3×10^5 cm 2 /V s close to the DP, see Figure 2f. Figure 2c,f represent the field-effect carrier mobility as a function of carrier concentration in graphene. The x-axis is the carrier concentration of graphene, which can be tuned from electron side (positive n) to hole side (negative n) by apply a gate voltage (V_g). The carrier fluctuation (referred as Δn) is determined by the fitting in Figure 2b,d. As shown in Figure 2c,f, the field-effect carrier mobility of graphene is carrier-concentration-dependent. The behavior of non-constant $\mu(n)$ may originate from different scattering efficiency for a particular type of defects in graphene. An alternative explanation consistent with the behavior of $\mu(n)$ is the renormalization of the Fermi velocity v_F , as previously observed in high-mobility suspended graphene devices [49–51]. In principle, the valence band (hole doping) and the conduction band (electron doping) are symmetric and the contribution of hole and electron to the carrier mobility is equal in in freestanding perfect

graphene sheet. As shown in Figure 2c,f, the extracted carrier mobilities of hole and electron are slight asymmetric, which may originate to the substrate-induced scattering and the electron-hole puddles in graphene. We also compared the device performance of graphene on different substrates, which is shown in Supplementary Material Section 4.

As shown in Figure 3a, under fixed gate voltage ($V_g = 0.5$ V) and low temperature ($T = 1.6$ K), the overall positive R_{xy} indicates that the contribution is mainly from electrons. Under a low magnetic field, the QHE shows clear Shubnikov-de Haas (SdH) oscillations. With the increase of the magnetic field, R_{xy} appears plateaus and R_{xx} is vanishing, which is the typical QHE [52,53]. Multiple plateaus are clearly observed in the R_{xy} measurements. For the filling factors $\nu = 2$ and $\nu = 6$, the magnetic fields range from 1.88 T to 2.36 T ($\nu = 2$) and from 0.77 T to 0.82 T ($\nu = 6$), respectively. Therefore, the $\nu = 2$ plateau has the widest range of magnetic field in all the R_{xy} plateaus, which can be utilized as the quantum resistance standard. In Figure 3b, we adjust V_g at a fixed magnetic field ($B = 1$ T) and low temperature ($T = 1.6$ K) to access the quantum Hall plateaus. The lowest point of longitudinal resistance R_{xx} corresponds to the plateaus of the Hall resistance, and the quantum Hall plateaus of $\nu = \pm 2, \pm 6, \pm 10, \pm 14, \pm 18$ are clearly observed. The QHE in graphene is different from the conventional QHE because the quantization is turned into a half integer, $R_{xy}^{-1} = \nu(e^2/h)$, where the filling factor $\nu = \pm 4(n + 1/2)$, n is a non-negative integer, the negative filling factor represents the quantum Hall effect (R_{xy}) in the hole doping regime, while it is positive for electron doping. In Figure 3c, we show the change of longitudinal resistance R_{xx} with the regulation of gate voltage (V_g) and magnetic field (B), in which we can see the typical fan of Landau levels. The black-colored areas indicate the vanish of R_{xx} , which means the Landau levels at these areas are clearly visible [54]. At magnetic field $B > 0.5$ T, $R_{xy}(B)$ exhibits plateaus and R_{xx} is vanishing, which are the hallmarks of the QHE. At least two well-defined plateaus with values $(2e^2/h)$ and $(6e^2/h)$, followed by a developing $(10e^2/h)$ plateau, are observed before the QHE features transform into SdH oscillations at a lower magnetic field. We observed the equivalent QHE features for holes with negative R_{xy} values. Alternatively, we can probe the QHE in both electrons and holes by fixing the magnetic field $B = 1$ T and changing V_g across the Dirac point. In this case, as V_g increases, first holes ($V_g < V_{DP}$) and later electrons ($V_g > V_{DP}$) fill successive Landau levels and exhibit the QHE, as shown in Figure 3b. For a fixed magnetic field, the periodicity of R_{xx} oscillation in carrier concentration is given by:

$$\Delta n = \alpha \Delta V_g = 4B/\Phi_0$$

where ΔV_g is the periodicity in gate voltage and $\Phi_0 = h/2e$ is the flux quanta. The factor “4” corresponds to the four-fold spin and valley degeneracy in graphene.

To further support the high performance of the device, we also measured the transport properties by changing the magnetic field at relatively high temperatures of 100 K and 150 K, and we observe that the device can also show hall plateau values of $h/\pm 2e^2$. As shown in Figure 4a, at the temperature of 100 K, with the continuous enhancement of the magnetic field, the hall plateau values of $h/\pm 2e^2$ are gradually obvious. Similarly, at the temperature of 150 K, the same phenomenon can be observed. The reason why the QHE can be observed at such high temperatures is the large cyclotron gaps of Dirac fermions in graphene, which is $\hbar\omega_c$. Their energy in the magnetic field is quantified as $E_N = v_F \sqrt{2e\hbar BN}$, where $v_F \approx 10^6$ m/s is the Fermi velocity and N is the integer of Landau level [21,23]. The energy gap at $B = 12$ T between $N = 0$ and ± 1 is $\Delta E \approx 1449$ K, which means that even with the high temperature of 150 K in our experiment, $\hbar\omega_c$ is about 10 times bigger than the thermal energy $k_B T$. We also measured at $T = 200$ K and $B = 12$ T, where we can barely see the quantum hall plateaus, see Figure S6. The higher the temperature goes, the more the mobility decreases, and we need a much stronger magnetic field to observe the QHE. Moreover, graphene devices have a very high carrier concentration occupied with a single 2D sub-band, which can completely fill the lowest Landau level under a high magnetic field; secondly, our graphene devices still have a high carrier mobility of 1×10^5 cm²/V·s at room temperature, which is proportional to scattering

time τ . Additionally, the scattering time of our device can reach $\tau \sim 10^{-12}$ s, so the condition of $\omega_c \tau = \mu \cdot B \gg 1$ can be reached at a low magnetic field of several T, compared with the Hall devices based on GaAs/AlGaAs heterostructures [3], HgTe quantum wells [55], and SiO₂ supported graphene [25], which usually require magnetic fields above 20 Tesla to achieve the quantum Hall effect above the nitrogen temperatures (>77 K). However, we cannot observe the plateaus at 100 K and 150 K with a too low magnetic field (0.1 T), see Figure S7. Generally speaking, in order to eliminate the influence of thermal fluctuation on the measurement, the observation of QHE requires a low temperature. On the one hand, we need to study quantum phenomena under extreme environmental conditions, while on the other hand, the more stable quantum state is also important for the actual measurement under relaxed experimental conditions.

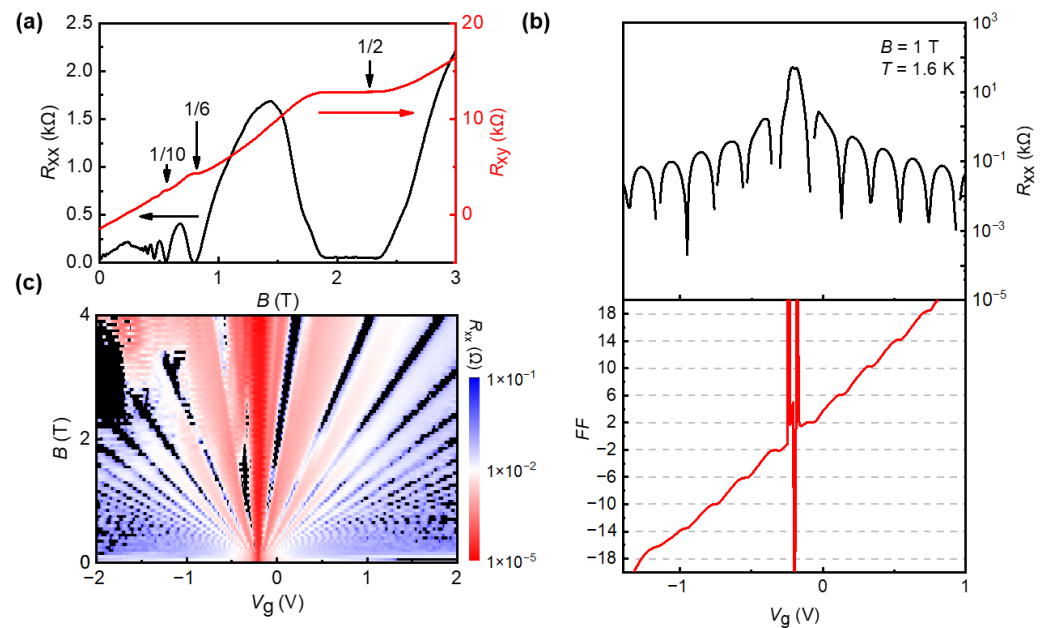


Figure 3. (a) Longitudinal resistance R_{xx} and Hall resistance R_{xy} as a function of magnetic field B at $V_g = 0.5$ V and $T = 1.6$ K. (b) Longitudinal resistance R_{xx} (black, top) and filling factor (FF) of R_{xy} (red, bottom) as a function of graphite-gate voltage at $T = 1.6$ K, $B = 1$ T. The horizontal dashed gray lines indicate the plateau values of the half-integer QHE. (c) False-color map of the longitudinal resistance R_{xx} of this device as a function of graphite-gate voltage (V_g) and magnetic field (B).

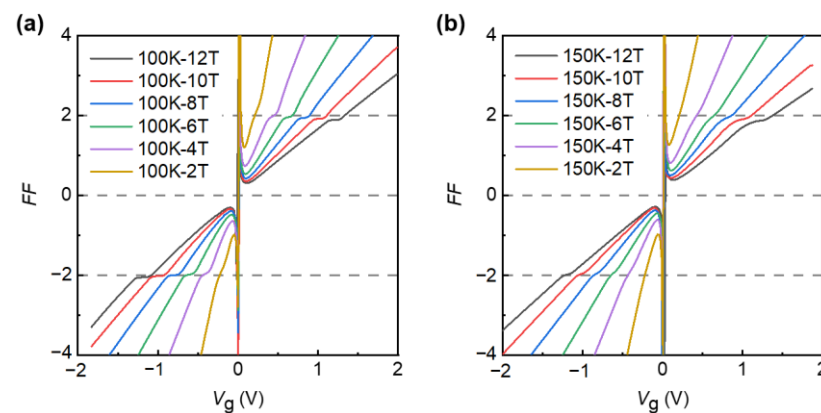


Figure 4. (a) Filling factor of R_{xy} as a function of graphite-gate voltage at $T = 100$ K in different magnetic field (from $B = 2$ T to 12 T). The horizontal gray lines indicate the hall plateau values of $h/\pm 2e^2$. (b) Same as (a), but measured at $T = 150$ K.

3. Conclusions

In summary, we report high-quality graphene field-effect devices by hBN encapsulation and local graphite bottom gate electrodes. Electrical transport experiments show that the graphene devices exhibit very high carrier mobility in both electron and hole sides. For the electron doping regime, the mobility exceeds $10^5 \text{ cm}^2/\text{V}\cdot\text{s}$ and $3 \times 10^5 \text{ cm}^2/\text{V}\cdot\text{s}$ at room temperature (290 K) and cryogenic temperature (1.6 K). The residual charge carrier fluctuation is only about 10^{10} cm^{-2} , indicating the great purity and homogeneity of the graphene devices. The well-defined low carrier concentration in graphene makes it ideal for an ultra-sensitive Hall sensor with a current-related sensitivity of $S_I \sim 500 \text{ V}/(\text{AT})$ at room temperature, which surpasses both silicon-based Hall sensors and the best Hall sensors based on III/V semiconductors. Further, benefiting from the high carrier mobility, the integer quantum Hall effect is finely developed in graphene under a perpendicular magnetic field below 1 T at low temperature. More surprisingly, clear quantum plateaus at $\nu = 2$ in graphene can even persist at an elevated temperature of 150 K, far above the liquid nitrogen temperature. At the same time, the required magnetic field for the high-temperature quantum Hall effect is only about 5 T, which can be realized by commercial superconducting solenoids. The relaxed conditions of quantum Hall effect in graphene, including high temperatures and small magnetic fields, will open new routes for the development of graphene-based resistance standards for the new *Système International d'unités*.

Supplementary Materials: The following supporting information can be downloaded at: <https://www.mdpi.com/article/10.3390/nano12213777/s1>, Figure S1: (a–c) Preparation of slide for transfer; Figure S2: (a–f) Fabrication process of hBN/MLG/hBN/FLG heterostructure; Figure S3: The method of electrical measurement; Figure S4: Graphene Hall bar devices on different substrates. Optical microscopy images of (a) graphene device on SiO_2 substrate and (b) hBN encapsulated graphene (Gr) device on graphite (Gra) local gate. Measured longitudinal resistivity of (c) SiO_2 -supported graphene device and (d) graphite-gated graphene device. V_{DP} refers to the gate voltage for the Dirac point of graphene; Figure S5: Carrier concentration dependence of transport properties of graphene devices on different substrates. The conductivity as a function of the charge carrier density n for (a) SiO_2 -supported graphene devices and (b) graphite-gated graphene device. The residual charge carrier fluctuation is calculated by the intercept of two lines. Carrier mobility μ as function of charge carrier density (c) SiO_2 -supported graphene devices and (d) graphite-gated graphene device; Figure S6: (a) R_{xx} and R_{xy} at 200 K under a big magnetic field of 12 T. (b) Filling Factor of R_{xy} as a function of graphite-gate voltage at $T = 200 \text{ K}$ and $B = 12 \text{ T}$; Figure S7: (a) R_{xy} and Filling Factor as a function of graphite-gate voltage at $T = 100 \text{ K}$ at $B = 0.1 \text{ T}$. (b) Same as (a) but measured at $T = 150 \text{ K}$. References [56,57] are cited in the supplementary materials.

Author Contributions: M.Z. conceived the idea and designed the experiments. S.Z. fabricated the devices with the help of Q.L. and Z.C. S.Z. carried out the transport measurements with the help of Y.X. C.G. and M.Z. supervised this project. S.Z. and M.Z. wrote the manuscript with the input of all authors. All authors have read and agreed to the published version of the manuscript.

Funding: This work is financially supported by the National Key R&D Program of China (No. 2018YFA0306900), the National Natural Science Foundation of China (No. 12174444), and the Natural Science Foundation of Hunan Province (No. 2020JJ3039 and 2020RC3032). We sincerely thank Zheng Han in Shanxi University for his great help in device fabrication and transport measurements.

Institutional Review Board Statement: Not applicable.

Informed Consent Statement: Not applicable.

Data Availability Statement: The data presented in this study are available on request from the corresponding author.

Conflicts of Interest: The authors declare no conflict of interest.

References

1. Klitzing, K.V.; Dorda, G.; Pepper, M. New method for high-accuracy determination of the fine-structure constant based on quantized Hall resistance. *Phys. Rev. Lett.* **1980**, *45*, 494–497. [\[CrossRef\]](#)
2. Halperin, B.I. Quantized Hall conductance, current-carrying edge states, and the existence of extended states in a two-dimensional disordered potential. *Phys. Rev. B* **1982**, *25*, 2185–2190. [\[CrossRef\]](#)
3. Delahaye, F.; Jeckelmann, B. Revised technical guidelines for reliable dc measurements of the quantized Hall resistance. *Metrologia* **2003**, *40*, 217. [\[CrossRef\]](#)
4. D’orio, M.; Wood, B.M. Temperature dependence of the quantum Hall resistance. *Surf. Sci.* **1986**, *170*, 233–237. [\[CrossRef\]](#)
5. Matthews, J.; Cage, M.E. Temperature Dependence of the Hall and Longitudinal Resistances in a Quantum Hall Resistance Standard. *J. Res. Natl. Inst. Stand. Technol.* **2005**, *110*, 497–510. [\[CrossRef\]](#)
6. Yu, R.; Zhang, W.; Zhang, H.J.; Zhang, S.C.; Dai, X.; Fang, Z. Quantized anomalous Hall effect in magnetic topological insulators. *Science* **2010**, *329*, 61–64. [\[CrossRef\]](#)
7. Chang, C.-Z.; Zhang, J.; Feng, X.; Shen, J.; Zhang, Z.; Guo, M.; Li, K.; Ou, Y.; Wei, P.; Wang, L.-L.; et al. Experimental Observation of the Quantum Anomalous Hall Effect in a Magnetic Topological Insulator. *Science* **2013**, *340*, 167–170. [\[CrossRef\]](#)
8. Chang, C.-Z.; Zhao, W.; Kim, D.Y.; Zhang, H.; Assaf, B.A.; Heiman, D.; Zhang, S.-C.; Liu, C.; Chan, M.H.; W.; Moodera, J.S. High-precision realization of robust quantum anomalous Hall state in a hard ferromagnetic topological insulator. *Nat. Mater.* **2015**, *14*, 473–477. [\[CrossRef\]](#)
9. Bestwick, A.J.; Fox, E.J.; Kou, X.; Pan, L.; Wang, K.L.; Goldhaber-Gordon, D. Precise quantization of the anomalous Hall effect near zero magnetic field. *Phys. Rev. Lett.* **2015**, *114*, 187201. [\[CrossRef\]](#)
10. Vonsovskii, S.V. *Magnetism*, 2nd ed.; John Wiley and Sons: New York, NY, USA, 1974.
11. Bedyazev, A.V.; Voloshinskii, A.N.; Granovskii, A.B.; Ryzhanova, N.V. Anomalous hall effect in disordered ferromagnetic alloys of the transition metals. *Sov. Phys. J.* **1987**, *30*, 1. [\[CrossRef\]](#)
12. Cohen, M.H.; Jortner, J. Effective medium theory for the Hall effect in disordered materials. *Phys. Rev. Lett.* **1973**, *30*, 696. [\[CrossRef\]](#)
13. Götz, M.; Fijalkowski, K.M.; Pesel, E.; Hartl, M.; Schreyeck, S.; Winnerlein, M.; Grauer, S.; Scherer, H.; Brunner, K.; Gould, C.; et al. Precision measurement of the quantized anomalous Hall resistance at zero magnetic field. *Appl. Phys. Lett.* **2018**, *112*, 72102. [\[CrossRef\]](#)
14. Fox, E.J.; Rosen, I.T.; Yang, Y.; Jones, G.R.; Elmquist, R.E.; Kou, X.; Pan, L.; Wang, K.L.; Goldhaber-Gordon, D. Part-per-million quantization and current-induced breakdown of the quantum anomalous Hall effect. *Phys. Rev. B* **2018**, *98*, 75145. [\[CrossRef\]](#)
15. Okazaki, Y.; Oe, T.; Kawamura, M.; Yoshimi, R.; Nakamura, S.; Takada, S.; Mogi, M.; Takahashi, K.S.; Tsukazaki, A.; Kawasaki, M.; et al. Precise resistance measurement of quantum anomalous Hall effect in magnetic heterostructure film of topological insulator. *Appl. Phys. Lett.* **2020**, *116*, 143101. [\[CrossRef\]](#)
16. Okazaki, Y.; Oe, T.; Kawamura, M.; Yoshimi, R.; Nakamura, S.; Takada, S.; Mogi, M.; Takahashi, K.S.; Tsukazaki, A.; Kawasaki, M.; et al. Quantum anomalous Hall effect with a permanent magnet defines a quantum resistance standard. *Nat. Phys.* **2022**, *18*, 25–29. [\[CrossRef\]](#)
17. Rigosi, A.F.; Elmquist, R.E. The quantum Hall effect in the era of the new SI. *Semicond. Sci. Technol.* **2019**, *34*, 93004. [\[CrossRef\]](#)
18. Milton, M.J.; Davis, R.; Fletcher, N. Towards a new SI: A review of progress made since 2011. *Metrologia* **2014**, *51*, R21. [\[CrossRef\]](#)
19. Janssen, T.J.; B.M.; Rozhko, S.; Antonov, I.; Tzalenchuk, A.; Williams, J.M.; Melhem, Z.; He, H.; Lara-Avila, S.; Kubatkin, S.; Yakimova, R. Operation of graphene quantum Hall resistance standard in a cryogen-free table-top system. *2D Mater.* **2015**, *2*, 35015. [\[CrossRef\]](#)
20. Kruskopf, M.; Bauer, S.; Pimsut, Y.; Chatterjee, A.; Patel, D.K.; Rigosi, A.F.; Elmquist, R.E.; Pierz, K.; Pesel, E.; Götz, M.; et al. Graphene Quantum Hall Effect Devices for AC and DC Electrical Metrology. *IEEE Trans. Electron Devices* **2021**, *68*, 3672–3677. [\[CrossRef\]](#)
21. Zhang, Y.; Tan, Y.W.; Stormer, H.L.; Kim, P. Experimental observation of the quantum Hall effect and Berry’s phase in graphene. *Nature* **2005**, *438*, 201–204. [\[CrossRef\]](#)
22. Ribeiro-Palau, R.; Lafont, F.; Brun-Picard, J.; Kazazis, D.; Michon, A.; Cheynis, F.; Couturaud, O.; Consejo, C.; Jouault, B.; Poirier, W.; et al. Quantum Hall resistance standard in graphene devices under relaxed experimental conditions. *Nat. Nanotechnol.* **2015**, *10*, 965–971. [\[CrossRef\]](#)
23. Novoselov, K.S.; Geim, A.K.; Morozov, S.V.; Jiang, D.; Katsnelson, M.I.; Grigorieva, I.V.; Dubonos, S.V.; Firsov, A.A. Two-dimensional gas of massless Dirac fermions in graphene. *Nature* **2005**, *438*, 197–200. [\[CrossRef\]](#)
24. Pezzini, S.; Mišeikis, V.; Pace, S.; Rossella, F.; Watanabe, K.; Taniguchi, T.; Coletti, C. High-quality electrical transport using scalable CVD graphene. *2D Mater.* **2020**, *7*, 041003. [\[CrossRef\]](#)
25. Novoselov, K.S.; Jiang, Z.; Zhang, Y.; Morozov, S.V.; Stormer, H.L.; Zeitler, U.; Maan, J.C.; Boebinger, G.S.; Kim, P.; Geim, A.K. Room-Temperature Quantum Hall Effect in Graphene. *Science* **2007**, *315*, 1379. [\[CrossRef\]](#)
26. Geim, A.K.; Grigorieva, I.V. Van der Waals heterostructures. *Nature* **2013**, *499*, 419–425. [\[CrossRef\]](#)
27. Dean, C.R.; Young, A.F.; Meric, I.; Lee, C.; Wang, L.; Sorgenfrei, S.; Watanabe, K.; Taniguchi, T.; Kim, P.; Shepard, K.L.; et al. Boron nitride substrates for high-quality graphene electronics. *Nat. Nanotechnol.* **2010**, *5*, 722–726. [\[CrossRef\]](#)

28. Wang, L.; Meric, I.; Huang, P.Y.; Gao, Q.; Gao, Y.; Tran, H.; Taniguchi, T.; Watanabe, K.; Campos, L.M.; Muller, D.A.; et al. One-Dimensional Electrical Contact to a Two-Dimensional Material. *Science* **2013**, *342*, 614–617. [\[CrossRef\]](#)
29. Gorbachev, R.V.; Geim, A.K.; Katsnelson, M.I.; Novoselov, K.S.; Tudorovskiy, T.; Grigorieva, I.V.; MacDonald, A.H.; Morozov, S.V.; Watanabe, K.; Taniguchi, T.; et al. Strong Coulomb drag and broken symmetry in double-layer graphene. *Nat. Phys.* **2012**, *8*, 896–901. [\[CrossRef\]](#)
30. Ponomarenko, L.A.; Gorbachev, R.V.; Yu, G.L.; Elias, D.C.; Jalil, R.; Patel, A.A.; Mishchenko, A.; Mayorov, A.S.; Woods, C.R.; Wallbank, J.R.; et al. Cloning of Dirac fermions in graphene superlattices. *Nature* **2013**, *497*, 594–597. [\[CrossRef\]](#)
31. Dean, C.R.; Wang, L.; Maher, P.; Forsythe, C.; Ghahari, F.; Gao, Y.; Katoch, J.; Ishigami, M.; Moon, P.; Koshino, M.; et al. Hofstadter’s butterfly and the fractal quantum Hall effect in moiré superlattices. *Nature* **2013**, *497*, 598–602. [\[CrossRef\]](#)
32. Hunt, B.; Sanchez-Yamagishi, J.D.; Young, A.F.; Yankowitz, M.; LeRoy, B.J.; Watanabe, K.; Taniguchi, T.; Moon, P.; Koshino, M.; Jarillo-Herrero, P.; et al. Massive Dirac Fermions and Hofstadter Butterfly in a van der Waals Heterostructure. *Science* **2013**, *340*, 1427–1430. [\[CrossRef\]](#) [\[PubMed\]](#)
33. Britnell, L.; Gorbachev, R.V.; Jalil, R.; Belle, B.D.; Schedin, F.; Mishchenko, A.; Georgiou, T.; Katsnelson, M.I.; Eaves, L.; Morozov, S.V.; et al. Field-Effect Tunneling Transistor Based on Vertical Graphene Heterostructures. *Science* **2012**, *335*, 947–950. [\[CrossRef\]](#)
34. Poirier, W.; Schopfe, F. Can graphene set new standards? *Nat. Nanotechnol.* **2010**, *5*, 171. [\[CrossRef\]](#) [\[PubMed\]](#)
35. Schaefer, B.T.; Wang, L.; Jarjour, A.; Watanabe, K.; Taniguchi, T.; McEuen, P.L.; Nowack, K.C. Magnetic field detection limits for ultraclean graphene Hall sensors. *Nat. Commun.* **2020**, *11*, 4163. [\[CrossRef\]](#) [\[PubMed\]](#)
36. Kretinin, A.V.; Cao, Y.; Tu, J.S.; Yu, G.L.; Jalil, R.; Novoselov, K.S.; Haigh, S.J.; Gholinia, A.; Mishchenko, A.; Lozada, M.; et al. Electronic Properties of Graphene Encapsulated with Different Two-Dimensional Atomic Crystals. *Nano Lett.* **2014**, *14*, 3270–3276. [\[CrossRef\]](#)
37. Zibrov, A.A.; Kometter, C.; Zhou, H.; Spanton, E.M.; Taniguchi, T.; Watanabe, K.; Zaletel, M.P.; Young, A.F. Tunable interacting composite fermion phases in a half-filled bilayer-graphene Landau level. *Nature* **2017**, *549*, 360–364. [\[CrossRef\]](#)
38. Rhodes, D.; Chae, S.H.; Ribeiro-Palau, R.; Hone, J. Disorder in van der Waals heterostructures of 2D materials. *Nat. Mater.* **2019**, *18*, 541–549. [\[CrossRef\]](#)
39. Zeng, Y.; Li, J.; Dietrich, S.A.; Ghosh, O.M.; Watanabe, K.; Taniguchi, T.; Hone, J.; Dean, C.R. High-Quality Magnetotransport in Graphene Using the Edge-Free Corbino Geometry. *Phys. Rev. Lett.* **2019**, *122*, 137701. [\[CrossRef\]](#)
40. Giovannetti, G.A.; K.P.; Khomyakov, P.A.; Brocks, G.; Karpan, V.V.; van den Brink, J.; Kelly, P.J. Doping graphene with metal contacts. *Phys. Rev. Lett.* **2008**, *101*, 026803. [\[CrossRef\]](#)
41. Xia, F.; Perebeinos, V.; Lin, Y.M.; Wu, Y.; Avouris, P. The origins and limits of metal–graphene junction resistance. *Nat. Nanotechnol.* **2011**, *6*, 179–184. [\[CrossRef\]](#)
42. Russo, S.; Craciun, M.F.; Yamamoto, M.; Morpurgo, A.F.; Tarucha, S. Contact resistance in graphene-based devices. *Phys. E Low-Dimens. Syst. Nanostruct.* **2010**, *42*, 677–679. [\[CrossRef\]](#)
43. Smith, J.T.; Franklin, A.D.; Farmer, D.B.; Dimitrakopoulos, C.D. Reducing contact resistance in graphene devices through contact area patterning. *ACS Nano* **2013**, *7*, 3661–3667. [\[CrossRef\]](#) [\[PubMed\]](#)
44. Robinson, J.A.; LaBella, M.; Zhu, M.; Hollander, M.; Kasarda, R.; Hughes, Z.; Trumbull, K.; Cavalero, R.; Snyder, D. Contacting graphene. *Appl. Phys. Lett.* **2011**, *98*, 053103. [\[CrossRef\]](#)
45. Yamaguchi, J.; Hayashi, K.; Sato, S.; Yokoyama, N. Passivating chemical vapor deposited graphene with metal oxides for transfer and transistor fabrication processes. *Appl. Phys. Lett.* **2013**, *102*, 143505. [\[CrossRef\]](#)
46. Lindvall, N.; Kalabukhov, A.; Yurgens, A. Cleaning graphene using atomic force microscope. *J. Appl. Phys.* **2012**, *111*, 64904. [\[CrossRef\]](#)
47. Schmitz, M.; Ouaj, T.; Winter, Z.; Rubi, K.; Watanabe, K.; Taniguchi, T.; Zeitler, U.; Beschoten, B.; Stampfer, C. Fractional quantum Hall effect in CVD-grown graphene. *2D Mater.* **2020**, *7*, 041007. [\[CrossRef\]](#)
48. Tanabe, S.; Sekine, Y.; Kageshima, H.; Nagase, M.; Hibino, H. Half-integer quantum Hall effect in gate-controlled epitaxial graphene devices. *Appl. Phys. Express* **2010**, *3*, 75102. [\[CrossRef\]](#)
49. Du, X.; Skachko, I.; Barker, A.; Andrei, E.Y. Approaching ballistic transport in suspended graphene. *Nat. Nanotechnol.* **2008**, *3*, 491–495. [\[CrossRef\]](#)
50. Bolotin, K.I.; Sikes, K.J.; Hone, J.; Stormer, H.L.; Kim, P. Temperature-Dependent Transport in Suspended Graphene. *Phys. Rev. Lett.* **2008**, *101*, 096802. [\[CrossRef\]](#)
51. Mayorov, A.S.; Elias, D.C.; Mukhin, I.S.; Morozov, S.V.; Ponomarenko, L.A.; Novoselov, K.S.; Geim, A.K.; Gorbachev, R.V. How Close Can One Approach the Dirac Point in Graphene Experimentally? *Nano Lett.* **2012**, *12*, 4629–4634. [\[CrossRef\]](#)
52. Jiang, Z.; Zhang, Y.; Tan, Y.W.; Stormer, H.L.; Kim, P. Quantum Hall effect in graphene. *Solid State Commun.* **2007**, *143*, 14–19. [\[CrossRef\]](#)
53. Li, L.; Yang, F.; Ye, G.J.; Zhang, Z.; Zhu, Z.; Lou, W.; Zhou, X.; Li, L.; Watanabe, K.; Taniguchi, T.; et al. Quantum Hall effect in black phosphorus two-dimensional electron system. *Nat. Nanotechnol.* **2016**, *11*, 593–597. [\[CrossRef\]](#) [\[PubMed\]](#)
54. Banszerus, L.; Schmitz, M.; Engels, S.; Dauber, J.; Oellers, M.; Haupt, F.; Watanabe, K.; Taniguchi, T.; Beschoten, B.; Stampfer, C. Ultrahigh-mobility graphene devices from chemical vapor deposition on reusable copper. *Sci. Adv.* **2015**, *1*, e1500222. [\[CrossRef\]](#) [\[PubMed\]](#)

-
55. Kozlov, D.A.; Kvon, Z.D.; Mikhailov, N.N.; Dvoretiskii, S.A.; Weishäupl, S.; Krupko, Y.; Portal, J.C. Quantum Hall effect in HgTe quantum wells at nitrogen temperatures. *Appl. Phys. Lett.* **2014**, *105*, 132102. [[CrossRef](#)]
 56. Kim, K.; Yankowitz, M.; Fallahazad, B.; Kang, S.; Movva, H.C.P.; Huang, S.; Larentis, S.; Corbet, C.M.; Taniguchi, T.; Watanabe, K.; et al. van der Waals Heterostructures with High Accuracy Rotational Alignment. *Nano Lett.* **2016**, *16*, 1989–1995. [[CrossRef](#)] [[PubMed](#)]
 57. Grenadier, S.; Li, J.; Lin, J.; Jiang, H. Dry etching techniques for active devices based on hexagonal boron nitride epilayers. *J. Vac. Sci. Technol. A Vac. Surf. Film.* **2013**, *31*, 061517. [[CrossRef](#)]